Simulation of high temperature thermal energy storage system based on coupled metal hydrides for solar driven steam power plants

Anna d'Entremont[1], Claudio Corgnale[1,2*], Bruce Hardy[1], Ragaiy Zidan[1]

1. Savannah River National Laboratory
2. Greenway Energy

Abstract

Concentrating solar power plants can achieve low cost and efficient renewable electricity production if equipped with adequate thermal energy storage systems. Metal hydride based thermal energy storage systems are appealing candidates due to their demonstrated potential for very high volumetric energy densities, high exergetic efficiencies, and low costs. The feasibility and performance of a thermal energy storage system based on $NaMgH_2F$ hydride paired with $TiCr_{1.6}Mn_{0.2}$ is examined, discussing its integration with a solar-driven ultra-supercritical steam power plant. The simulated storage system is based on a laboratory-scale experimental apparatus. It is analyzed using a detailed transport model accounting for the thermochemical hydrogen absorption and desorption reactions, including kinetics expressions adequate for the current metal hydride system. The results show that the proposed metal hydride pair can suitably be integrated with a high temperature steam power plant. The thermal energy storage system achieves output energy densities of 226 kWh/m^3, 9 times the DOE SunShot target, with moderate temperature and pressure swings. In addition, simulations indicate that there is significant scope for performance improvement via heat-transfer enhancement strategies.

---

[*] Corresponding author. Tel.: +1 803 617 9689.
E-mail address: claudio.corgnale@greenway-energy.com (C. Corgnale).

Nomenclature and abbreviations

Abbreviations

CSP	Concentrating solar power
DOE	US Department of Energy
GWE	Greenway Energy
HTMH	High-temperature metal hydride
LTMH	Low-temperature metal hydride
MH	Metal hydride
SRNL	Savannah River National Laboratory
TES	Thermal energy storage
USC	Ultra super critical
TIT	Turbine inlet temperature

Variables

C_a	Preexponential absorption kinetics factor (s^{-1})
C_d	Preexponential desorption kinetics factor (s^{-1})
C_P	Specific heat capacity at constant pressure (J/kg·K)

E_a	Absorption activation energy (J/mol)
E_d	Desorption activation energy (J/mol)
ΔH	Enthalpy of reaction for H_2 desorption (J/mol)
h	Molar enthalpy of H_2 (J/mol)
k	Thermal conductivity (W/m·K)
L	Fill length of MH in test vessel cavity (m)
M_{H2}	Molecular weight of H_2 (kg/g-mol)
n_M	Molar H_2 storage capacity of MH bed (mol)
P	Gas pressure (Pa)
P_{atm}	Atmospheric pressure (Pa)
P_{eq}	Equilibrium pressure between the MH and the gas (Pa)
$\dot{q}$	Volumetric thermal power input (W/m^3)
Q	Thermal energy input (J)
$\dot{Q}$	Thermal power input (W)
R	Universal gas constant (J/mol·K)
R_v	Radius of MH cavity in test vessel (m)

S	Mass rate of production of H_2 gas (kg/m^{3}s)
ΔS	Entropy of reaction (J/mol·K)
T	Temperature (K)
t	Time (s)
$\vec{v}$	Gas velocity vector (m/s)
$\vec{v}_s$	Superficial gas velocity vector (m/s)
X	Molar concentration of H_2 absorbed within the MH (mol/m^3)
X_m	Minimum molar concentration of H_2 in MH (mol/m^3)
X_M	Maximum molar concentration of H_2 in MH (mol/m^3)
ε	Porosity of the MH bed
η	Efficiency
η_d	Dilatational viscosity of H_2 gas (Pa·s)
μ	Dynamic viscosity of H_2 gas (Pa·s)
ρ	Mass density (kg/m^3)
$\underline{\underline{\tau}}$	Viscous stress tensor (Pa)

Subscripts

$H2$	Associated with H_2 gas
$HTMH$	Associated with high-temperature metal hydride
$LTMH$	Associated with low-temperature metal hydride
MH	Associated with metal hydride (same value for both HTMH and LTMH)
$MHBulk$	Associated with bulk (non-porous) MH material (same value for both HTMH and LTMH)
PP	Associated with power plant
SS	Associated with stainless steel
0	Initial condition

1 Introduction

One of the best solutions to produce renewable electric power is represented by concentrating solar power (CSP) plants [1], due to their potential to provide highly dispatchable power [2-5]. However, to achieve low electricity production costs, CSP plants must be coupled with suitable thermal energy storage (TES) systems [6]. With an adequate storage system, the plant can produce electricity continuously at a power level dictated mainly by the plant capacity factor. Currently thermal energy can be stored as sensible heat, latent heat, or thermochemical heat [2-3].

Thermochemical systems utilizing coupled metal hydrides (MHs) are a very appealing option due to the high efficiency, high energy density and potential low costs [7,8, 9,10]. Recent analyses have demonstrated that MH-based TES systems can achieve volumetric energy densities almost 10 times larger than traditional molten salt systems [7]. They also have the potential for high exergetic efficiencies, on the order of 95%, and lower costs than molten salt systems, approaching the DOE target of 15 $/kWhth [7,8,11]. A MH-based TES system requires a high-temperature metal hydride (HTMH) to be paired with a low-temperature metal hydride (LTMH). Among the HTMH materials available for TES applications, those based on Na and Mg show several positive characteristics. The Na and Mg class of materials operates at temperatures on the order of 500-650 °C, depending on the MH formulation [7,11,12]. This range of temperatures makes the TES system suitable for integration with solar driven high pressure or supercritical steam power plants, which usually operate at temperatures on the order of 600 °C [13,14]. The Na-Mg metal hydrides have also demonstrated the capability to reach high energy densities [7], high exergetic efficiencies [7,11] and relatively low investment costs [7]. The materials best suited for TES applications and currently available are $NaMgH_3$ and NaH. A third Na-Mg MH formulation, the $NaMgH_2F$ material, is being actively examined for thermal energy storage applications. This material was extensively studied and characterized by Bouamrane et al in the late 1990's [15]. Recent investigations have demonstrated the high potential of $NaMgH_2F$ for thermal energy storage use. The material has shown the potential to reach TES system cost lower than 30 $/kWhth when the HTMH is coupled with sodium alanate based LTMH [11,12]. The reduced system cost can be attributed mainly to the low raw material cost and the high reaction enthalpy of 96.8 $kJ/molH_2$ [11,12]. The TES system based on $NaMgH_2F$ can also reach exergetic efficiencies on the order of 86% [11] and TES system volumetric energy densities on the order of 240 $kWhth/m^3$, i.e. about 10 times larger than the DOE target of 25 $kWhth/m^3$ [7,12]. However the initial formulation of this material showed some drawbacks relative to the cycling performance, with a remarkable cycling degradation after only a few cycles [11]. This issue has recently been solved with some minor material modifications as discussed and demonstrated in Ref [16].

The present work focuses on the technical assessment and performance analysis of a TES system comprising the $NaMgH_2F$ HTMH material, coupled with a high pressure Ti based LTMH ($TiCr_{1.6}Mn_{0.2}$). This coupled TES system can achieve operating temperatures of about 600-650 °C, requiring low temperature heat at about 15-30 °C. This makes the proposed TES system suitable for integration with a CSP plant based on an ultra-supercritical (USC) steam cycle operating at approximately 600°C.

The objective of this work is also aimed to identify the setup and operating conditions for an optimized system configuration. To accomplish this, a laboratory-scale apparatus is simulated using a detailed transport model accounting for mass, energy and momentum balances, as well as kinetics expressions for the MH materials. The predicted spatial and temporal variation of the temperatures, gas pressure, and absorbed hydrogen concentration for the coupled MHs is presented and analyzed. The results obtained from the simulation will be used to guide future laboratory scale experimental tests and to identify optimal operating conditions for the integrated solar power plant at larger scales.

2 Solar driven plant concept

The proposed thermal energy storage system was selected to be integrated with a solar driven USC steam power plant, operating at temperatures on the order of 600-650 °C. The simplified schematic of the overall solar plant is shown in Figure 1.

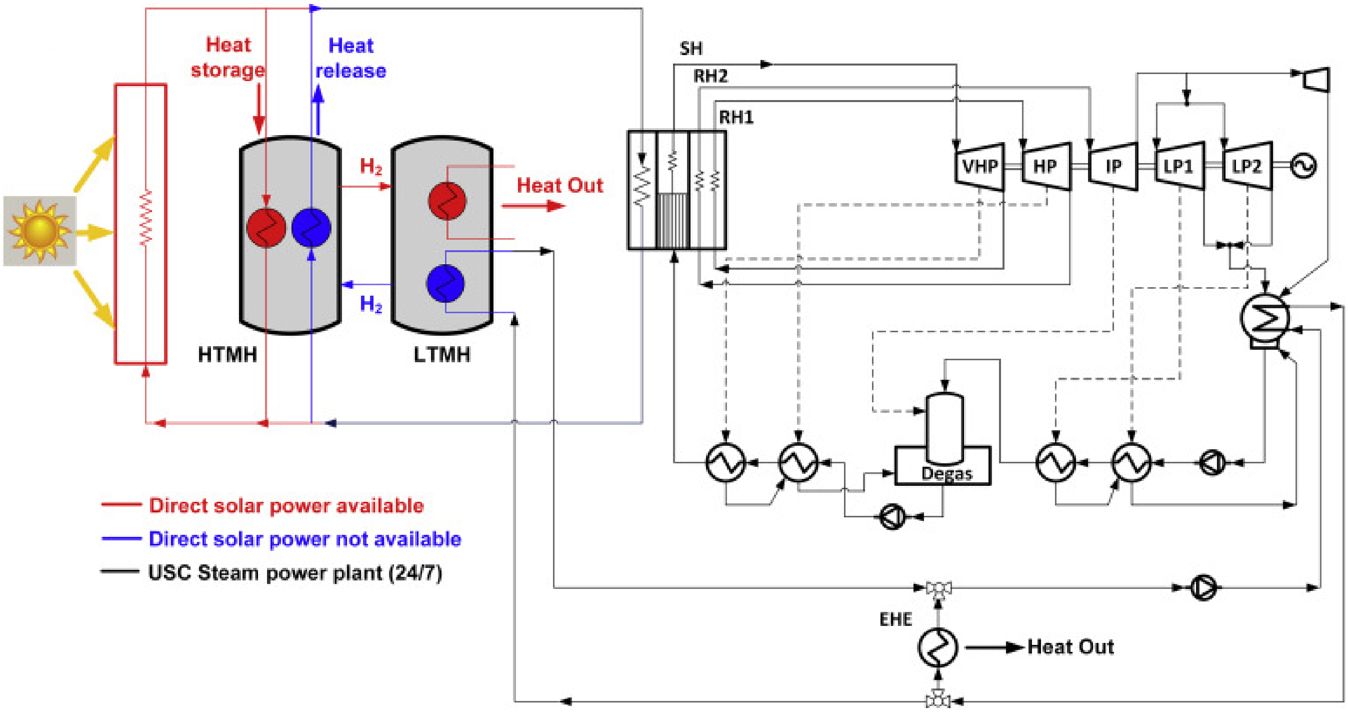

Figure 1: Solar driven USC steam power plant with MH based TES system

The plant is comprised of a solar capturing and concentrating section, a TES system based on coupled MHs (referred to as HTMH and LTMH) and a USC steam power plant, operating continuously.

The TES system cycles hydrogen between a high-temperature metal hydride (HTMH), operating at approximately the steam turbine inlet temperature, and a low-temperature metal hydride (LTMH), making use of the endothermic desorption and exothermic absorption reactions in each MH. During the day, when direct solar power is available, the steam power plant is driven by direct concentrated solar power. The surplus solar energy is stored in the TES system. The high temperature heat is exchanged with the HTMH (i.e. $NaMgH_2F$ material), which releases the hydrogen through an endothermic reaction. The desorbed hydrogen is stored in the LTMH through a low temperature exothermic reaction. The low temperature heat is rejected from the TES to the environment. When the power plant requires additional power the process is reversed. The hydrogen previously stored in the LTMH is absorbed in the HTMH providing the required high temperature thermal power. The low temperature heat required by the LTMH to desorb the hydrogen is provided by the waste heat available in the condenser of the power plant. More details on the principles of MH-based TES systems can be found in Ref [7].

The choice of an adequate LTMH is critical since the material needs to match both the HTMH operating conditions and the power plant waste heat properties. An initial screening of potential LTMH materials has been carried out based on the cost and the operating conditions of the material. The optimal LTMH should work at hydrogen pressures on the order of 50 bar, required to hydrogenate the HTMH, with operating temperatures on the order of 15-30 °C, allowing the power plant waste heat recovery. In addition, a self-sustaining plant concept must satisfy the following constraint: $\Delta H_{LTMH} < \Delta H_{HTMH} (1-\eta_{PP})$ where ΔH is the enthalpy of reaction for the absorption/desorption reaction and η_{PP} is the efficiency of the power plant.

This is a necessary, but not sufficient condition[†], which ensures that the waste thermal power, rejected from the steam power plant at constant temperature, can be sufficient to desorb the required hydrogen flow rate from the LTMH. The selected HTMH material has a reaction enthalpy of 96.8 kJ/molH_2 [12] and a typical USC steam power plant can reach cycle efficiencies on the order of 45-50% [13]. As a consequence, the selected LTMH needs to have reaction enthalpies at least lower than 45-50 kJ/molH_2. The Ti based $TiCr_{1.6}Mn_{0.2}$ material has been chosen as the coupled LTMH since it meets the required operating conditions and is characterized by a relatively low cost compared to other more expensive LTMH candidates. The power plant schematic is shown on the right hand side of Figure 1. The power required for steam generation is entirely provided by the solar source either directly or after storage in the TES. The USC steam feeds the steam turbine, which has five stages: (1) very high pressure (VHP)

[†] The condition has been assessed for the thermal energy release process (i.e. hydrogen absorption in the HTMH) with the following assumptions: (1) the MHs operate at constant temperature during the thermal energy release, (2) no additional losses (in the connecting equipment, tubing, etc) are included, (3) all the waste heat from the power plant can be recovered and used in the TES

stage operating at turbine inlet temperature (TIT) on the order of 600 °C and pressure of about 300 bar [13,14]; (2) high pressure (HP) stage operating at about the same TIT as the VHP stage and pressure of about 90 bar, after the first reheating (RH1) in the steam generator; (3) intermediate pressure (IP) stage operating at pressure of about 40 bar and same TIT of the high pressure stages, achieved after the second reheating (RH2); (4) low pressure stages (LP1 and LP2) where the steam expands reaching temperatures on the order of 40 °C (as required by the TES system) at a pressure of about 0.075 bar. The power plant has 5 regeneration lines (shown as dotted lines in Figure 1) to increase the efficiency as well as a degas unit to remove the air in the circuit at low pressures. The heat available from the condenser is recovered to release the hydrogen from the LTMH during the thermal energy release or is rejected to the environment (EHE heat exchanger) when direct solar power is available (Figure 1).

3 Methods and Analysis

3.1 Transport model

The transport model for the paired-MH TES system consists of mass, momentum, and energy balance equations, as well as the equation of state for gaseous hydrogen and kinetics expressions representing the H_2 absorption and desorption in the HTMH and the LTMH. The differential equations were solved using a finite element analysis approach in COMSOL Multiphysics.

3.1.1 Hydrogen transport

The mass balance for hydrogen gas accounts for gas flow and for H_2 production/consumption due to reactions with the MH. It must be solved in both the free gas spaces, such as the connecting tubes and open channels in the vessels, and within the porous MH beds. It can be expressed by the differential equations

$$\begin{cases} \dfrac{\partial \rho}{\partial t} + \nabla \cdot (\rho \vec{v}) = 0, & \text{in free gas volume} \\ \varepsilon \dfrac{\partial \rho}{\partial t} + \nabla \cdot (\rho \vec{v}_s) = S, & \text{in porous MH beds} \end{cases} \tag{1}$$

where ρ and $\vec{v}$ are respectively the density and actual velocity of the H_2 gas, ε is the porosity of the MH bed, and $\vec{v}_s = \varepsilon \vec{v}$ is the superficial gas velocity. The mass rate of hydrogen production S is expressed as

$$S = -M_{H2} \frac{\partial X}{\partial t} \tag{2}$$

where M_{H2} is the molar mass of hydrogen and X is the local molar concentration of H_2 absorbed in the MH.

The differential form of the momentum balance equation (Brinkman equation) for hydrogen flowing inside the media under laminar flow conditions is expressed as follows:

$$\frac{\rho}{\varepsilon} \frac{\partial \vec{v}_s}{\partial t} + \left(\frac{\mu}{\kappa} + \frac{S}{\varepsilon^2} \right) \vec{v}_s = -\nabla P + \nabla \cdot \left[\frac{\mu}{\varepsilon} \left(\nabla \vec{v}_s + \nabla \vec{v}_s^{\,T} \right) \right] - \nabla \cdot \left[\left(\frac{2\mu}{3} - \eta_d \right) \left(\frac{1}{\varepsilon} \right) \left(\nabla \cdot \vec{v}_s \right) \underline{\underline{I}} \right] \tag{3}$$

with P being the pressure, μ being the dynamic viscosity, and η_d being the dilatational viscosity of the H_2 gas.

This equation also includes the viscous stress term expressed in terms of velocity components, taking into account the viscosity of the media as well.

For free flows without porous media (such as the hydrogen connecting tubes and open channels in the tank), the porosity ε equals unity and the momentum balance equation under laminar conditions simplifies to:

$$\rho \frac{D\vec{v}}{Dt} = -\nabla P - \nabla \cdot \underline{\underline{\tau}} \tag{4}$$

The pressure P and gas density ρ are related via the hydrogen equation of state. The present model evaluates the hydrogen state using the ideal gas equation of state modified with the compressibility factor $Z(P,T)$:

$$P = Z(P,T)\rho RT \qquad (5)$$

The compressibility factor was evaluated by fitting data available from the NIST database [17].

3.1.2 Energy balance

The energy balance within the MH beds was assessed based on the local enthalpy balance accounting for both the MH material and the gaseous hydrogen within the pores. Approximating the hydrogen in the pores as an ideal gas, the molar enthalpy is taken as a function of temperature only, i.e., $h_{H2} = h_{H2}(T)$. As a result, the molar enthalpy terms can be expressed in terms of the specific heat capacity C_p and the temperature according to $dh = (\partial h/\partial T)|_p\, dT = (C_p/M_{H2})dT$. The resulting energy equation is expressed as

$$\rho_{MHBulk} C_{MH} \frac{\partial T}{\partial t} - \nabla \cdot \left(k(\vec{\nabla} T) \right) = -\varepsilon \rho_{H2} C_{PH2} \left(\frac{\partial T}{\partial t} + \vec{v} \cdot \vec{\nabla} T\right) + \varepsilon \frac{\partial P}{\partial t} + C_{PH2} T \cdot S + S \cdot \Delta H + \dot{q} \qquad (6)$$

where C_{MH} is the specific heat of the MH material, C_{PH2} is the hydrogen specific heat, k is the overall thermal conductivity, ΔH is the enthalpy of reaction, and $\dot{q}$ represents the contribution of any additional volumetric heat sources. Equation 6 is the general energy balance equation in a medium reacting with a fluid, accounting for pressure work and viscous dissipation [18]. However, the terms related to the kinetic energy and work done by gravitational force are neglected. This allows the pressure terms to be decoupled from the velocity terms, resulting in simplification of the differential equation integration and reduction of computational time.

For free hydrogen gas flowing outside the porous material, the energy balance equation is expressed as

$$\rho_{H2} C_{PH2} \frac{\partial T}{\partial t} - \nabla \cdot k \nabla T = -\rho_{H2} C_{PH2} \vec{v} \cdot \nabla T - \frac{T}{\rho_{H2}} C_{PH2} \left(\frac{\partial P}{\partial t} + \vec{v} \cdot \nabla P \right) - \underline{\underline{\tau}} : \nabla \vec{v} \qquad (7)$$

3.1.3 Reaction kinetics

A first order kinetics expression was adopted to simulate hydrogen absorption/desorption in the HTMH and LTMH materials:

$$\frac{dX}{dt} = \begin{cases} C_a \exp\left(-\frac{E_a}{RT}\right) ln\left(\frac{P}{P_{eq}}\right)(X_M - X), & P > P_{eq} \text{ (absorption)} \\ C_d \exp\left(-\frac{E_d}{RT}\right)\left(\frac{P - P_{eq}}{P_{eq}}\right)(X - X_m), & P < P_{eq} \text{ (desorption)} \end{cases} \qquad (8)$$

with C_a and C_d being the pre-exponential kinetics factors and E_a and E_d being the activation energies for H_2 absorption and desorption respectively and X_M and X_m being respectively the maximum and minimum molar concentrations of absorbed H_2 within the MH material.

The first expression of Equation 9 represents the hydrogen absorption kinetics at pressures higher than the equilibrium pressure, while the second expression represents the hydrogen desorption kinetics when pressures are lower than the equilibrium pressure.

The equilibrium pressure of the HTMH and LTMH was assessed adopting the van't Hoff equation

$$P_{eq} = P_{atm} \exp\left(\frac{\Delta H}{RT} - \frac{\Delta S}{R}\right) \qquad (9)$$

where P_{atm} is atmospheric pressure and ΔS is the entropy of reaction.

The current model assumes no slope in the bi-phase region and no hysteresis for the absorption/desorption process. Additional correction factors that will account for these phenomena will be included in the future work when the model results will be validated with experimental results.

3.2 Bench-scale paired MH system

The proposed MH-based system is numerically simulated using the transport model described previously. The material properties of the MHs as well as the initial and boundary conditions applied for the differential equations are based on an experimental apparatus available at the SRNL and GWE laboratories.

3.2.1 Experimental setup and material properties

Figure 2 shows the overall bench-scale experimental system (left), a close-up view of one of the MH test vessels (middle), and the corresponding vessel geometry used in the numerical simulations (right). The experimental system is designed to allow two metal hydrides to be directly tested at operational temperature and pressures. Details of the system were described in Ref. [18].

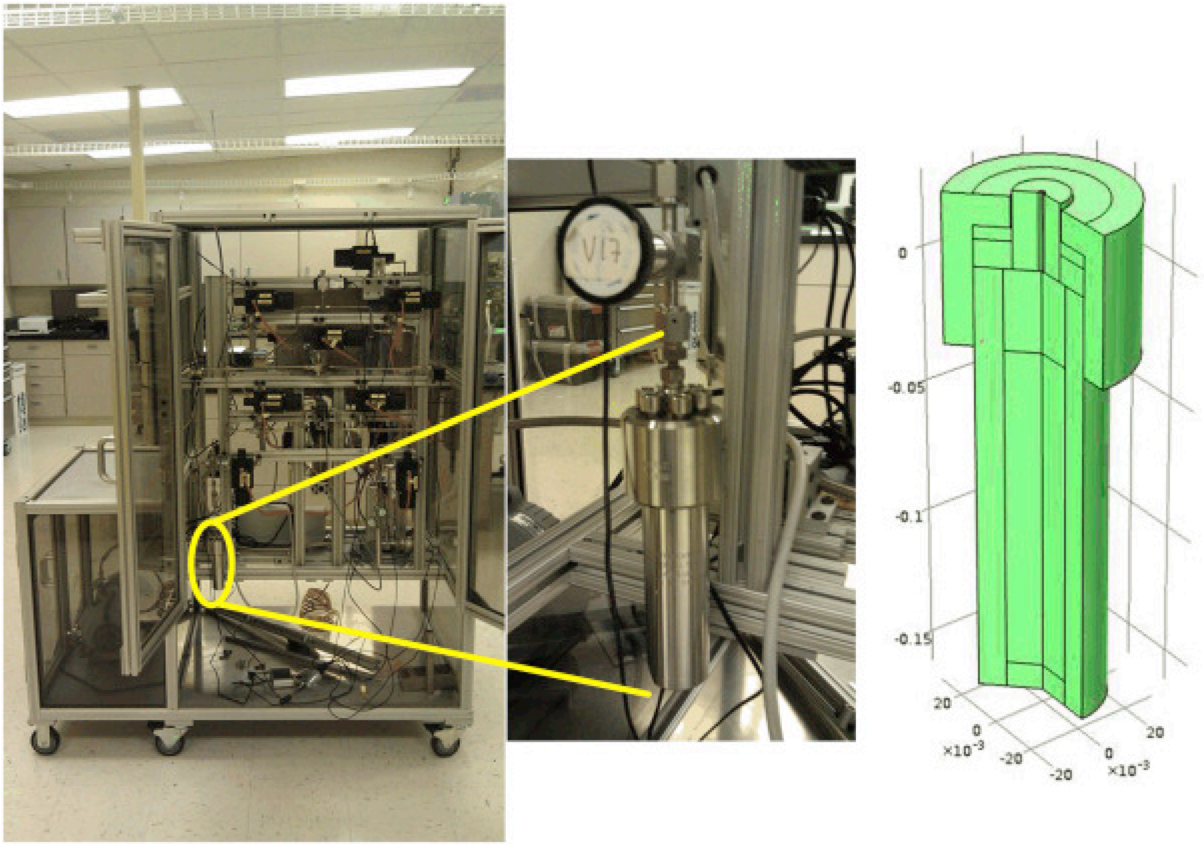

Figure 2: Bench scale apparatus for pairing two metal hydride beds (left), image of one of the metal hydride reactors (middle), modeling geometry of the sample vessel (right).

The thermodynamic and physical properties of the MH materials are summarized in Table 1. The values of reaction enthalpy and entropy are those reported in Reference [12]. The density values have been calculated based on the crystal density and the bed porosity, assumed equal to 50%. The value of the weight capacity, specific heat and the thermal conductivity of the two materials are typical values for the two selected materials and have been assumed based on the data reported in References [12,19,20].

Table 1: Properties of HTMH ($NaMgH_2F$) and LTMH ($TiCr_{1.6}Mn_{0.2}$) materials

Property	Units	HTMH ($NaMgH_2F$)	LTMH ($TiCr_{1.6}Mn_{0.2}$)	
ΔH	J/mol	–96800	–28000	Reaction enthalpy
ΔS	J/mol·K	–138.0	–129.0	Reaction entropy
ρ	kg/m^3	1390	3123	Bulk density
c_p	J/kg·K	1300	500	Specific heat
k_{tot}	W/m·K	0.5	0.6	Overall thermal conductivity of H_2-filled MH bed
ϵ		0.5	0.5	Porosity of bed
$wt\%$	kgH_2/kgMaterial	2.5	1.5	Weight capacity

3.2.2 Numerical model implementation

3.2.2.1 Model geometry

The numerical model geometry consisted of two identical stainless steel MH vessels connected by a short tube for H_2 gas transfer between them. The two vessels and the connecting tube were aligned axially to yield an axisymmetric system that could be modeled in two dimensions, r and z. Figure 3 shows the 2D axisymmetric geometry simulated. It was divided into regions of stainless steel, free hydrogen gas, and porous MH beds. Ten locations, indicated in Figure 3(a), were selected for plotting local results for temperature and equilibrium pressure. These locations were chosen as representative of the behavior in the core and outer surfaces of the MH beds. The dimensions of the vessels are shown in Figure 3(b).

Experimentally, the MH beds consist of a fill of MH powder with void space between particles to be filled with hydrogen gas. Numerically, the beds were represented homogeneous cylinders with uniform porosity and effective properties. The MH powder was assumed to uniformly fill the vessel cavity up to a specified distance, with free H_2 gas filling the remainder of the cavity. The fill length of MH powder in the vessel was denoted as L_{LTMH} for the LTMH and L_{HTMH} for the HTMH.

The geometry of the experimental stainless steel vessels was replicated as closely as possible in the model, while the connecting tubing was shortened (to 8.4 cm) and simplified. Because the shortened tube would result in an unrealistically large conductive heat transfer through the stainless steel tube wall connecting the vessels, the tube wall was omitted from the model and replaced by an adiabatic boundary condition.

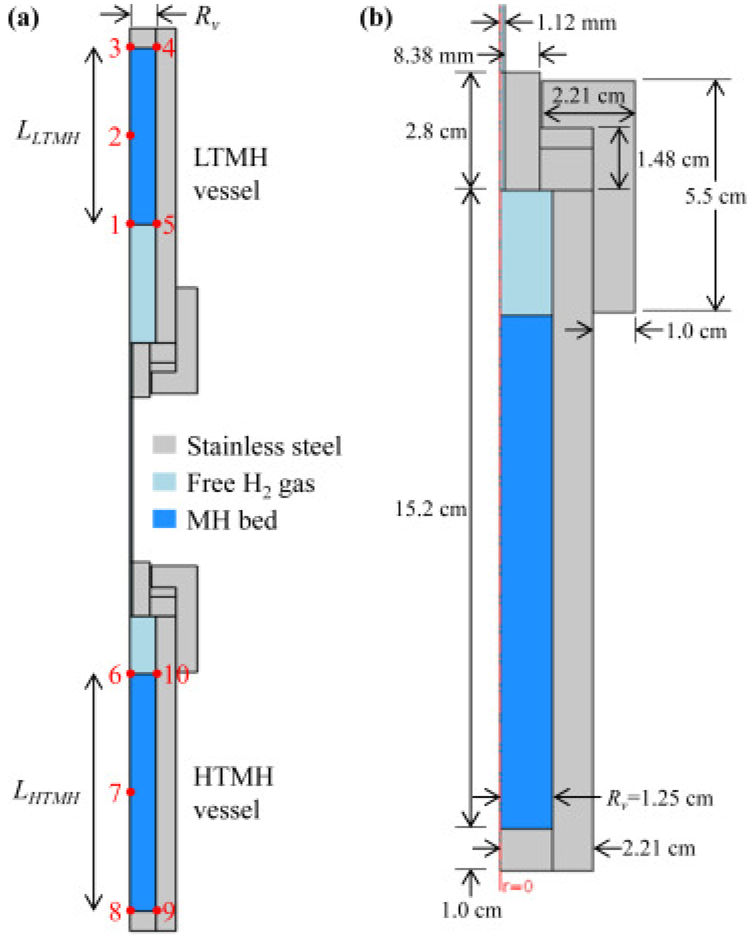

Figure 3: 2D axisymmetric model geometry, showing the inner radius R_v of the vessel cavity and the fill lengths L_{LTMH} and L_{HTMH} of the LTMH and HTMH beds, respectively. Local temperatures and equilibrium pressures will be plotted at the 10 state points within the LTMH and HTMH beds.

3.2.2.2 Boundary and initial conditions

The energy conservation equations (6-7) governing the temperature T are first-order in time and second-order in space. Therefore, they require one initial condition and two boundary conditions for the temperature T in each direction. The kinetics equation (8) governing the absorbed hydrogen concentration X inside each MH are first order in time, so they require one initial condition within each MH. The mass conservation equation (1) (first-order in time and space) and the momentum equations (3-4) (first order in time and second-order in space), governing the pressure P and gas velocity $\vec{v}$, require one initial condition and two boundary conditions in each direction.

Initially, the temperature T of the entire HTMH vessel, including the stainless steel as well as the MH and hydrogen contained inside, was uniform and equal to $T_{0,HTMH} = 640°\text{C}$. Similarly, the initial temperature of the LTMH vessel was uniform and equal to $T_{0,LTMH} = 14°\text{C}$. The temperature along the tube connecting the two vessels varied linearly in the z-direction from $T_{0,HTMH}$ at the bottom to $T_{0,LTMH}$ at the top. The absorbed hydrogen concentration X within each MH was initially uniform and equal to $X_{0,HTMH} = 0.95\ X_{M,HTMH}$ and $X_{0,LTMH} = 0.05\ X_{M,LTMH}$ in the HTMH and the LTMH, respectively. Here, the total amount of hydrogen initially absorbed in the two MHs equals the maximum capacity n_M of either single MH. The gas pressure was initially uniform throughout the entire system and equal to the equilibrium pressure of the HTMH, i.e., $P_0 = P_{eq,HTMH}(T_{0,HTMH})$, while the gas velocity $\vec{v}$ was zero everywhere.

Because the system is axisymmetric and solved in two dimensions, boundary conditions are required only in the radial r and axial z-directions. At the system centerline $r = 0$, axial symmetry existed for all variables, i.e., $\partial T/\partial r\ (r = 0) = 0$, $\partial P/\partial r\ (r = 0) = 0$, and $u_r(r = 0) = 0$. No slip and no penetration boundary conditions existed for the H_2 gas on all interior walls of the vessel at all times, i.e., $\vec{v}|_{wall} = \mathbf{0}$ and $\nabla P|_{wall} = 0$. The cap of each vessel and the connecting tube were thermally insulated on their outer surfaces at all times. During discharging of each MH, the entire outer surface of the vessel was thermally insulated while a volumetric heat source $\dot{q}$ was applied to the MH to represent the effects of the heaters in the bench-scale apparatus. During charging of the MH, a constant and uniform temperature, equal to $T_{0,HTMH}$ and $T_{0,LTMH}$ for the HTMH and LTMH vessels, respectively, was imposed on the outer wall and bottom of the vessel.

3.2.2.3 Sizing of the coupled MH bench scale system

To avoid excess cost and system volume, the two MH beds should be sized so they have the same theoretical maximum hydrogen storage capacity $n_{M,i}$ (in mol H_2). As shown in Ref. [18], for MH vessels with the same cavity radius R_v, the fill lengths L_{LTMH} and L_{HTMH} for the HTMH and LTMH, respectively, are related by

$$L_{LTMH} = \left(\frac{X_{M,HTMH}}{X_{M,LTMH}}\right) L_{HTMH} \qquad (10)$$

where $X_{M,LTMH}$ and $X_{M,HTMH}$ are the maximum H_2 concentrations for the LTMH and HTMH. In the present study, the HTMH is 1.35 times the volume of the LTMH. To maintain a free gas space in each cavity equal to at least 20% of the cavity volume, the HTMH volume was set to $L_{HTMH} = 0.8L_v = 0.122$ m, resulting in a LTMH fill length of $L_{HTMH} = 0.0905$ m and a theoretical H_2 storage capacity of $n_M = 1.04$ mol.

3.2.2.4 Heater power calculation

The heater power supplied to each MH bed during H_2 discharging must provide sufficient thermal energy for the H_2 desorption reaction. In addition, there must be a drop in equilibrium pressure between the discharging metal hydride and the charging metal hydride to drive H_2 between them. One or both of the metal hydrides must change temperature in order to reverse the direction of H_2 flow, and the heater powers must also account for the thermal energy for this sensible heating.

For each metal hydride, the thermal energy $Q_{rxn,i}$ (in J) required for desorption of the full H_2 capacity (n_M) can be computed based on the enthalpy of reaction ΔH_i as $Q_i = n_M \Delta H_i$ with $i = HTMH$ or $i = LTMH$. In the present model, the required thermal energies are $Q_{rxn,LTMH} = 29.135$ kJ and $Q_{rxn,HTMH} = 100.73$ kJ.

The thermal energy inputs required to raise the temperature of the LTMH, the HTMH, or one of the stainless steel (SS) vessels by a temperature difference ΔT can be computed as $Q_{i,\Delta T} = \rho_i V_i C_{P,i} \Delta T$, where ρ_i, V_i, and $c_{p,i}$ are the density, volume, and specific heat for material $i = LTMH, HTMH,$ or SS. For the materials in the present study, these evaluate to $Q_{LTMH,\Delta T} = (67.564 \text{ J/K})\Delta T$, $Q_{HTMH,\Delta T} = (108.22 \text{ J/K})\Delta T$, and $Q_{SS,\Delta T} = (1147 \text{ J/K})\Delta T$. Thus, the majority of the energy for sensible heating is devoted to raising the temperature of the stainless steel vessel. This can be attributed to the relatively large ratio of stainless steel volume to MH volume in the benchscale system. The fraction of energy input used to heat the vessel should decrease significantly as the system is scaled up.

The thermal energy input to each metal hydride is provided as a constant thermal power input $\dot{Q}_{h,i}$ over the 1.5 h discharging step, i.e., $\dot{Q}_{h,i} = (Q_{rxn,i} + Q_{i,\Delta T} + Q_{SS,\Delta T})/(1.5 \text{ h})$. In order to assess the system performance independent of heater placement, the simulation represented the heater power using a uniformly distributed volumetric heat source given by $\dot{q}_{h,i} = \dot{Q}_{h,i}/(\pi R_v^2 L_i)$. Therefore, the $\dot{q}$ term in the energy equation (6) is given by

$$\dot{q} = \begin{cases} \dot{q}_{h,LTMH} & \text{in LTMH bed during LTMH discharging} \\ \dot{q}_{h,HTMH} & \text{in HTMH during HTMH discharging} \\ 0 & \text{otherwise} \end{cases} \tag{11}$$

3.2.2.5 Target temperature ranges

Since the TES is integrated with a supercritical steam power plant, the target temperature range for the HTMH side of the cycle is 630–650°C to achieve a TIT on the order of 600-620 °C [13,14]. The LTMH heat input would ideally be provided by waste heat from the condenser, i.e., on the order of 15-30°C, with a low temperature that requires minimal active cooling.

During HTMH discharging (analogous to “daytime” operation when excess solar power is available for storage), the target temperature for the HTMH is 650°C. Assuming uniform temperature within each

MH, the system would be in equilibrium for a LTMH temperature of 18.9°C, i.e., $P_{eq,HTMH}(650°\mathrm{C}) = P_{eq,LTMH}(18.9°\mathrm{C})$ (Equation 9). The LTMH set point during this step was set at 14°C, about 5°C below the equilibrium value, to drive H_2 flow from the HTMH to the LTMH.

During HTMH charging (analogous to "nighttime" operation when the power plant operates from stored energy), the HTMH setpoint was 640°C. The corresponding equilibrium temperature in the LTMH would be about 15.5°C. The LTMH target temperature during this step was set to 24°C, about 9°C above the equilibrium value, to drive H_2 flow from the HTMH to the LTMH. As a result, the heater power for each MH bed accounted for sensible heating of $\Delta T = 10℃$.

3.2.2.6 Meshing

The computational domain was meshed using COMSOL's physics-based mesh settings with the predefined "Fine" element size, corresponding to maximum element size 2.46 cm, minimum element size 0.139 mm, maximum element growth rate of 1.3, and curvature factor 0.3 for the simulated geometry. The final mesh consisted of 15717 elements, with the finest elements along the interior surface of the vessel cavity to resolve the boundary layer and the coarsest elements on the outer edges of the vessel.

To assess mesh independence, the results using the mesh described above were compared with those of an identical model meshed using COMSOL's "Finer" predefined element size (max. element size 1.72 cm, min. element size 0.058 mm, max. element growth rate 1.25, and curvature factor 0.25) over one full cycle. This mesh refinement more than doubled the number of elements to 40202. The maximum relative errors in the predicted pressure, local temperatures, and amount of hydrogen in the HTMH were less than 0.5% at all times. The maximum relative error in the amount of hydrogen in the LTMH was less than 2% at all times, corresponding to less than 0.002 mol absolute error.

4 Results and Discussion

4.1 Individual MH characterization

4.1.1 MH absorption/desorption kinetics under constant temperature and pressure

The kinetics parameter values for the first-order kinetics expression given in Equation (8) are reported in Table 2 for both $NaMgH_2F$ and $TiCr_{1.6}Mn_{0.2}$.

Table 2: Kinetics parameters for the HTMH ($NaMgH_2F$) and LTMH ($TiCr_{1.6}Mn_{0.2}$) materials

	HTMH ($NaMgH_2F$)	LTMH ($TiCr_{1.6}Mn_{0.2}$)
Ca (1/s)	120000	25.0
Ea ($J/molH_2$)	102500	21500
Cd (1/s)	1000000	15.5
Ed ($J/molH_2$)	151500	19000
X_M ($molH_2/m^3$)	17375	23423
X_m ($molH_2/m^3$)	0	0

The kinetics parameters for both metal hydrides were assessed using a MathCad® optimization tool to fit the available data.

The LTMH material parameters were assessed based on the data and considerations reported in Reference [19]. The selected LTMH material has similar kinetics behavior as the other Ti based LTMH materials, as shown in Reference [19]. The HTMH material parameters were assessed using the optimization tool to match the available experimental data. HTMH absorption kinetics tests have been carried out at GWE and SRNL at temperature of 380 °C (with a hydrogen pressure of 40 bar) and 491 °C (with a hydrogen pressure of 51 bar). The values of the activation energy were measured experimentally for both charging and discharging, while the other kinetics parameters were assessed fitting the experimental data. Regarding the desorption kinetics, a behavior similar to the other Mg-Na based materials at the same corresponding conditions has been assumed. The numerically predicted LTMH absorption and desorption behavior is shown in Figure 4(a) (absorption) and Figure 4(b) (desorption). At an operating pressure of 60 bar, a temperature swing of 15–30°C during the charging/discharging process ensures an almost complete absorption and desorption within about one hour. This makes the material suitable for the current solar power plant conditions. A comparison of the experimental and numerical results for the HTMH absorption and desorption is shown in Figure 4(c) (absorption) and Figure 4(d) (desorption). The HTMH material shows good kinetics for both charging and discharging at operating temperatures on the order of 650°C and pressures on the order of 50-60 bar.

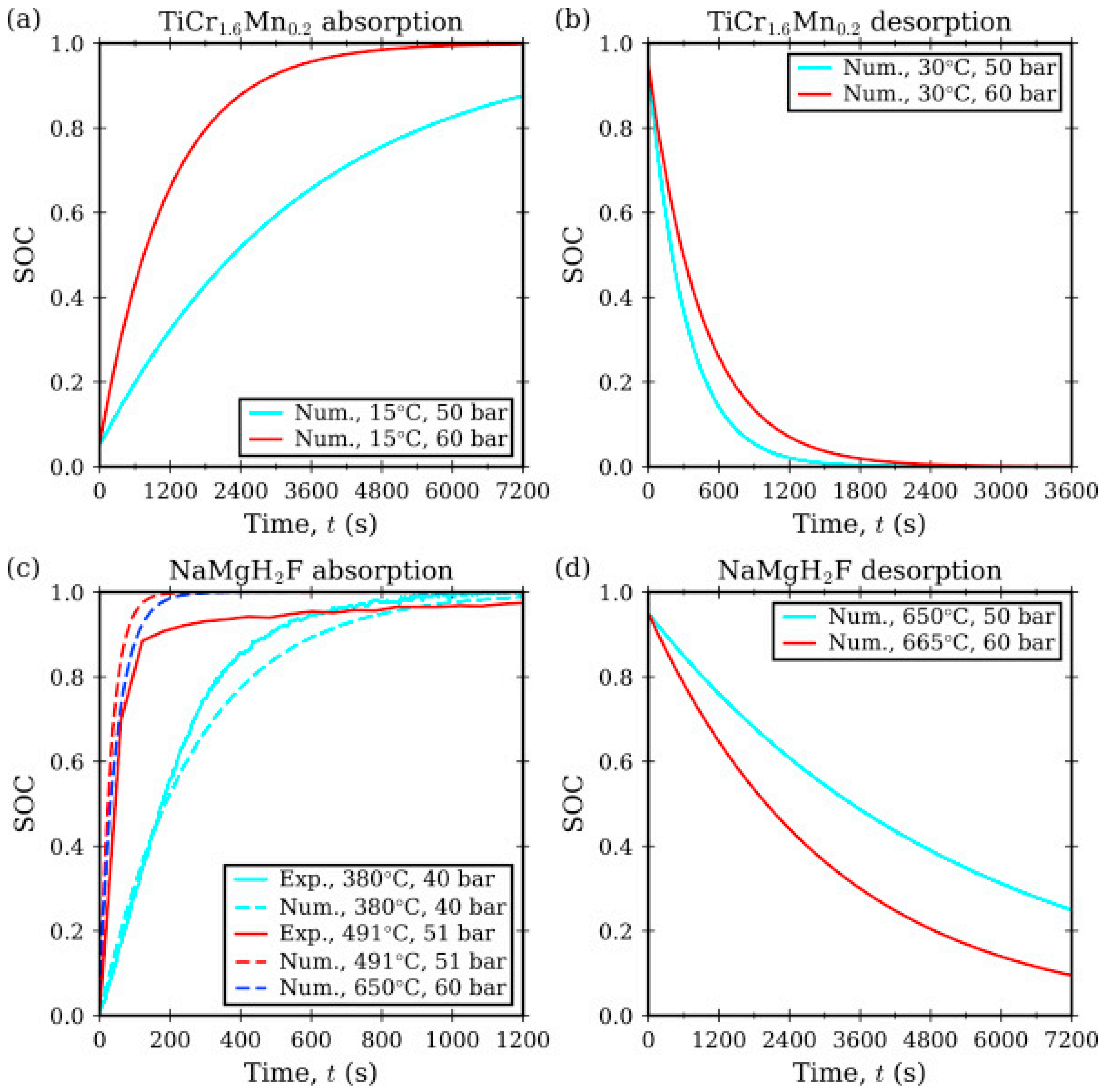

Figure 4: Predicted (a) absorption and (b) desorption kinetics for $TiCr_{1.6}Mn_{0.2}$ as well as (c) predicted and experimentally measured absorption and (d) predicted desorption kinetics for $NaMgH_2F$.

4.2 Model results for bench-scale paired MH system

4.2.1 Model temperature profiles

Figure 5 shows the average MH temperature $\bar{T}$ and local temperatures at selected locations within (a) the LTMH (locations 1–5) and (b) the HTMH (locations 6-10). The 10 locations are indicated in Figure 3, and were selected to illustrate the behavior within the core of the MH bed and on its surfaces in contact with the stainless steel vessel or free H_2 gas. Local temperatures ranged from 14°C to 43°C in the

LTMH and from 640°C to 689°C in the HTMH. The maximum temperatures in both MH beds occurred on the centerline ($r = 0$), roughly $0.25L_i$ from the bottom of the vessel. Temperatures T_2 and T_7 in the center of the MH beds (slightly lower than the maximum) are representative of the maximum temperature evolution. The minimum temperatures in each bed occurred at location 5 in the LTMH and location 10 in the HTMH, just inside the SS casing on the interface between the metal hydride and the free H_2 gas. In general, the temperature along the outer surface of the bed (represented by locations 3, 4, and 5 in the LTMH and 8, 9, and 10 in the HTMH) was close to uniform and significantly cooler than the interior of the metal hydride bed. In fact, the temperatures at the two locations in contact with the end of the vessel (locations 3 and 4 in the LTMH and 8 and 9 in the HTMH) were nearly identical at all times (<0.3% relative difference), so these curves overlap in the figure.

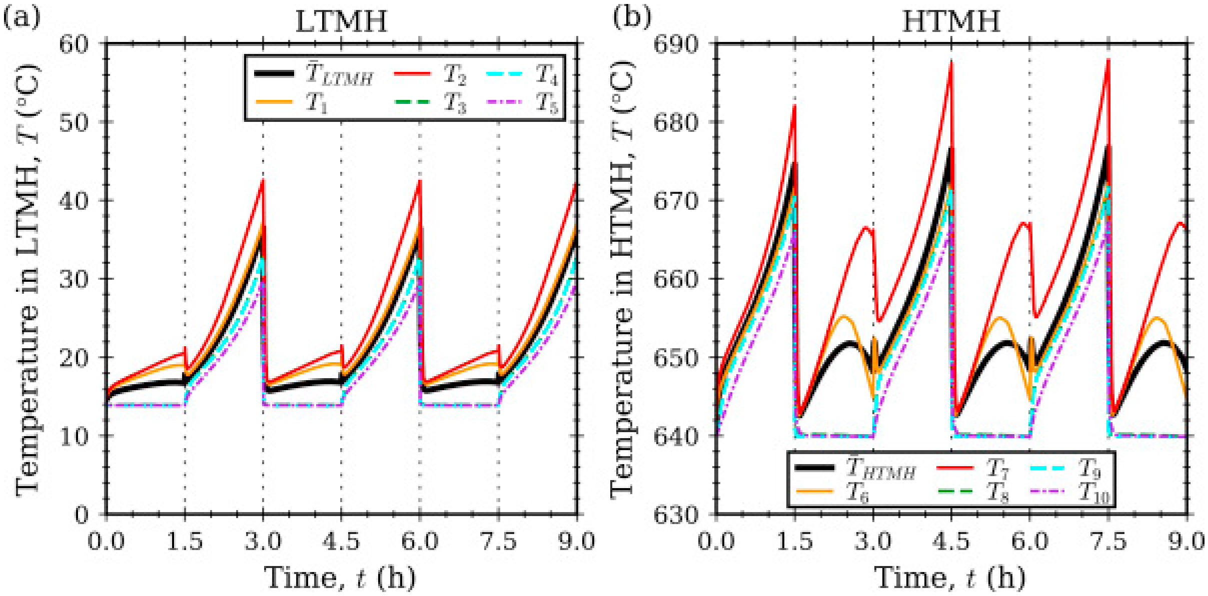

Figure 5: Average MH temperature and local temperature for selected locations as a function of time in (a) the LTMH and (b) the HTMH. The LTMH temperatures varied within an approximately 30°C range, while the range of HTMH temperatures was approximately 48°C. In both beds, the temperatures at locations in contact with the end of the vessel (locations 3 and 4 in the LTMH and 8 and 9 in the HTMH) were nearly identical at all times (<0.3% relative difference), so these curves overlap.

Each MH bed steadily rose in temperature throughout its discharging step due to the heater input. The charging step for each metal hydride began with an abrupt temperature drop due to the imposed temperature condition on the outside of the vessel. During this step, locations in contact with the stainless steel vessel (3–5 in the LTMH and 8–10 in the HTMH) were equal to the imposed temperature due to the high thermal conductivity of the vessel, while the temperatures along the MH centerline were larger due to the heat released by the exothermic absorption reaction.

4.2.2 Model pressure profiles

Figure 6 shows the pressure P of the hydrogen gas as well as the average equilibrium pressures $\bar{P}_{eq,LTMH}$ and $\bar{P}_{eq,HTMH}$ of the LTMH and TMH, respectively. The gas pressure remained approximately uniform throughout the entire system, including the free gas volume and the porous beds, over the entire simulation. The pressure drop required to drive gas flow in the system was on the order of 100 Pa and was negligibly small compared to the temporal variation in gas pressure or the difference $P_{eq,i} - P$ driving the absorption/desorption reactions. Over a full cycle, the pressure varied from 4.9 to 6.8 MPa (a 1.9 MPa range). Each step began with an abrupt pressure drop that can be attributed to rapid hydrogen absorption in the charging MH bed following the rapid temperature decrease (Figure 5). The absorption reaction depleted the free gas in the system until the discharging MH bed reached a high enough temperature to desorb hydrogen at a rate equal to or exceeding the rate of absorption. For most of the cycle, the gas pressure remained roughly halfway between the average equilibrium pressures of the MH beds.

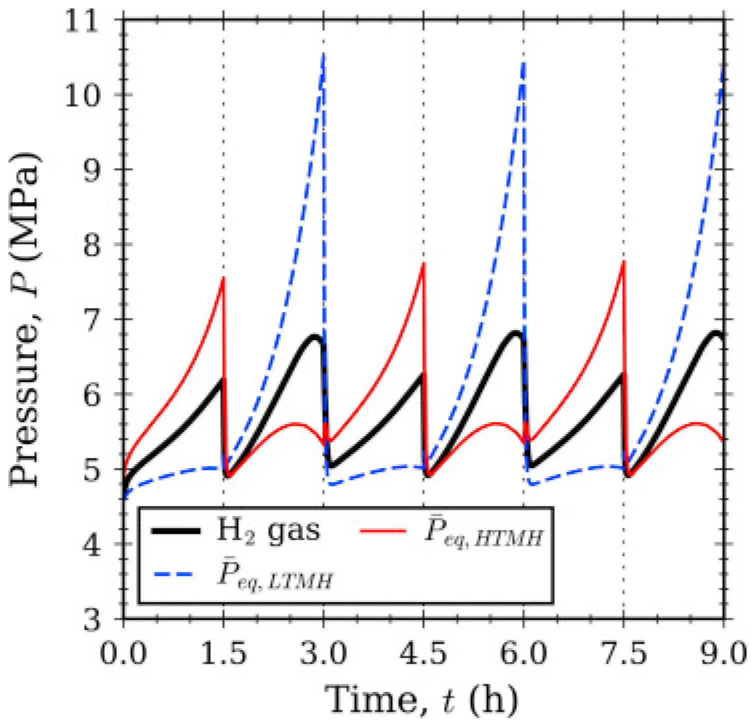

Figure 6: Pressure profile of the hydrogen gas and average equilibrium pressures $\bar{P}_{eq,LTMH}$ and $\bar{P}_{eq,HTMH}$ for the LTMH and HTMH beds, respectively, as functions of time over three cycles. The gas pressure was nearly uniform throughout the entire gas volume, and was roughly halfway between the average equilibrium pressures for the majority of the cycle.

Figure 7 shows the local equilibrium pressures at selected locations within (a) the LTMH and (b) the HTMH as well as the gas pressure as functions of time. The equilibrium pressure evolution at each location qualitatively resembles the temperature evolution, since the two quantities are linked via the van't Hoff equation (9). However, the range of equilibrium pressure in each metal hydride differs due to the differences in the reaction enthalpy and entropy of the two materials. Specifically, the LTMH equilibrium pressures varied over a much larger range than those in the HTMH despite having a smaller temperature range (Figure 5). This is a useful characteristic of the LTMH material, because it enables a relatively small temperature swing in the LTMH to provide a driving force for changing the direction of hydrogen flow in the system.

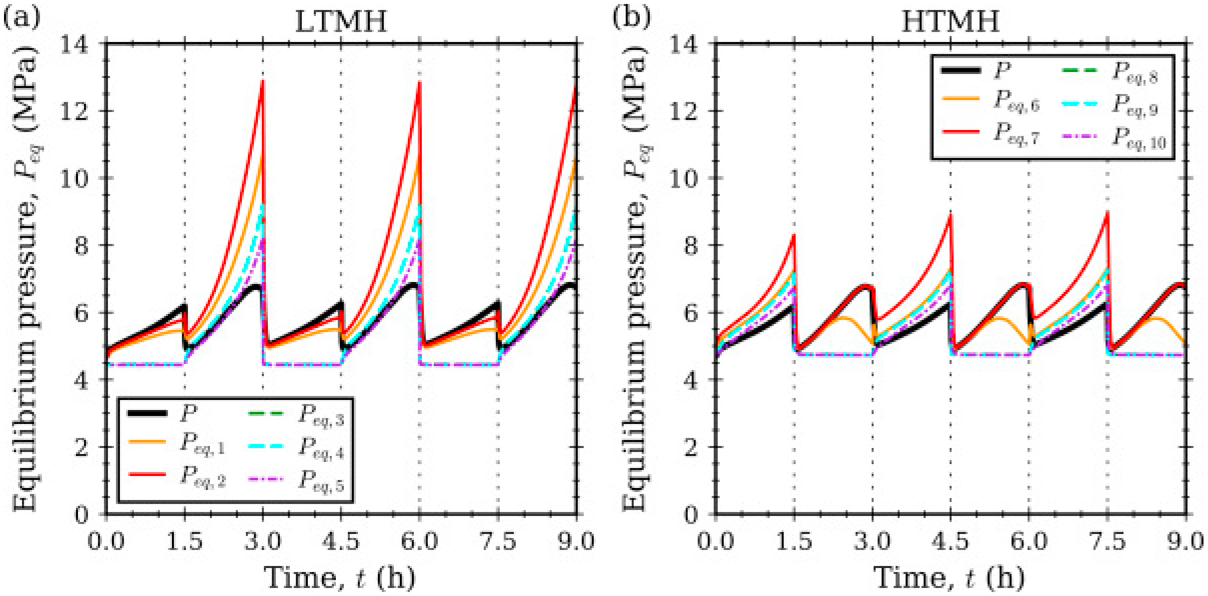

Figure 7: Local equilibrium pressures P_{eq} at selected locations as functions of time within (a) the LTMH and (b) the HTMH as well as the gas pressure P. In both beds, the equilibrium pressures at locations in contact with the end of the vessel (locations 3 and 4 in the LTMH and 8 and 9 in the HTMH) were nearly identical at all times (≤0.3% relative difference), so these curves overlap.

4.2.3 Hydrogen transport and MH state of charge (SOC)

Figure 8 shows (a) the flowrate of H_2 gas leaving each MH bed and (b) the amount of H_2 contained in the LTMH, the HTMH, and the gas as functions of time. The H_2 content in (b) is represented in moles on the left-hand axis and as the state of charge (SOC), i.e., the percentage of the theoretical bed capacity n_M, on the right-hand axis.

For the majority of the cycle, the rates of absorption and desorption [Figure 8(a)] were approximately equal to one another. However, at the beginning of each step, the rapid temperature drop in the charging MH bed (Figure 5) caused the H_2 absorption rate to increase more rapidly than the desorption rate in the discharging bed. This accounts for the abrupt pressure drops observed at the beginning of each step in Figure 6.

Both the absorption and desorption flowrates decreased towards the end of a step, particularly at the end of HTMH charging steps. This can be attributed to the hydrogen content in the MH beds approaching saturation or depletion. As the absorbed hydrogen concentration in the metal hydride approaches the maximum concentration (during absorption) or the minimum concentration (during desorption), the kinetics expression indicates that the reaction rate will decrease. Figure 8(b) shows that the HTMH charging step nearly saturates the HTMH and almost completely depletes the hydrogen content of the LTMH, while the LTMH charging step reaches approximately 80% of the HTMH capacity and lowers the LTMH content to approximately 16% of capacity. Overall, about 77% of the system capacity was cycled in and out of the HTMH bed.

Figure 8(b) demonstrates that that the two metal hydrides form a balanced system that yielded consistent cycling behavior starting from the first cycle with negligible thermal ratcheting.

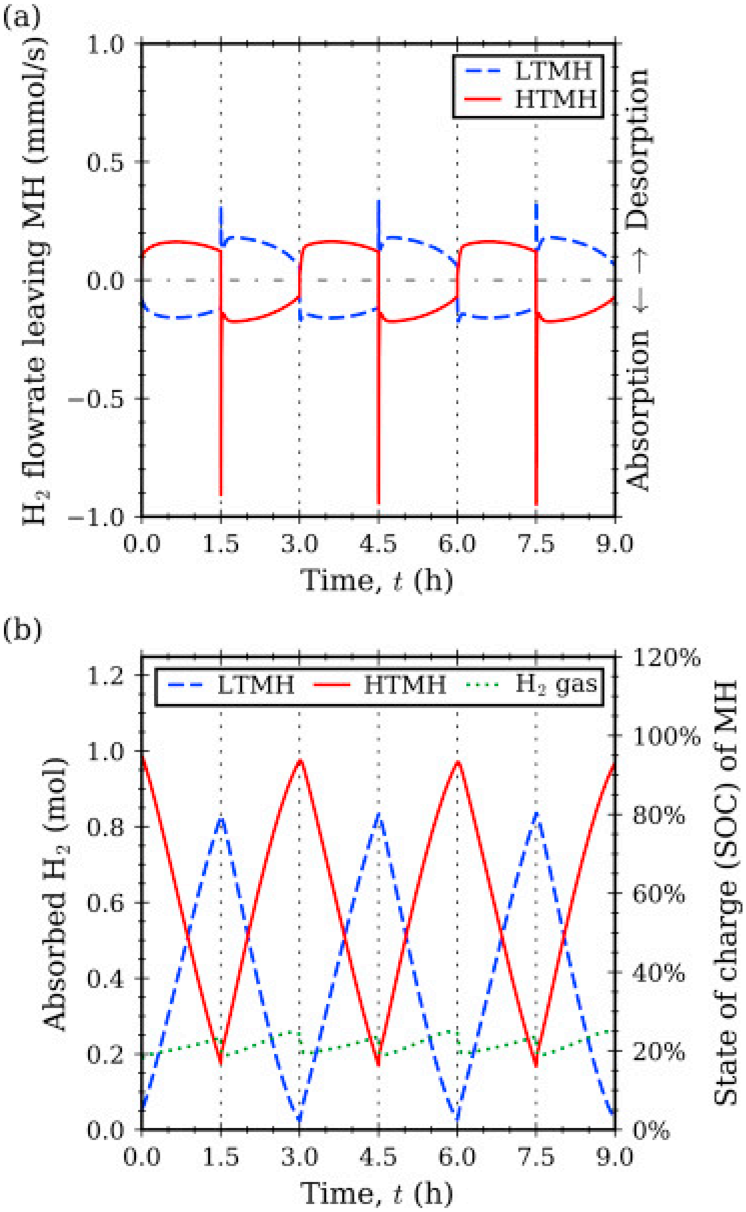

Figure 8: (a) The molar flowrate of H_2 gas exiting each MH bed and (b) the amount of H_2 stored in the HTMH, LTMH, and in gaseous form as functions of time. The corresponding state of charge of each MH bed is shown in the right-hand axis of (b).

4.2.4 System energy density

Figure 9 shows the rates of heat transfer into and out of the HTMH, i.e., the heat input supplied by the heater during LTMH charging, the heat output from the HTMH to the vessel during HTMH charging, and the time-averaged heat output, as functions of time. Approximately 75% of the heat input during LTMH charging was retrieved during HTMH charging. The output energy density was $\frac{E_{HTMH,out}}{V_{HTMH}+V_{LTMH}} =$

226 kWh/m^3, where $E_{HTMH,out}$ is the total thermal energy output over the HTMH charging step and $V_i = \pi R_v^2 L_i$ is the volume of a MH bed. This energy density is about 9 times the SunShot target of 25 kWh/m^3.

At the beginning of the HTMH charging steps, the heat output reached a large peak with a maximum value of 157 W. This period of rapid heat transfer lasted only about two minutes before the rate of heat output dropped below 20 W. It can be attributed to the use of the imposed temperature boundary condition, which rapidly cooled the vessel, as previously observed in Figure 5(b). Following this rapid cooling, the HTMH heat output reached a local maximum of 18 W about 15 minutes after the start of the HTMH charging step and decreased for the remainder of the step. The evolution of the heat output follows the same shape as the magnitude of the HTMH hydrogen absorption rate shown in Figure 8(a), and the decrease in heat output can similarly be attributed to approaching full depletion of the LTMH and saturation of the HTMH.

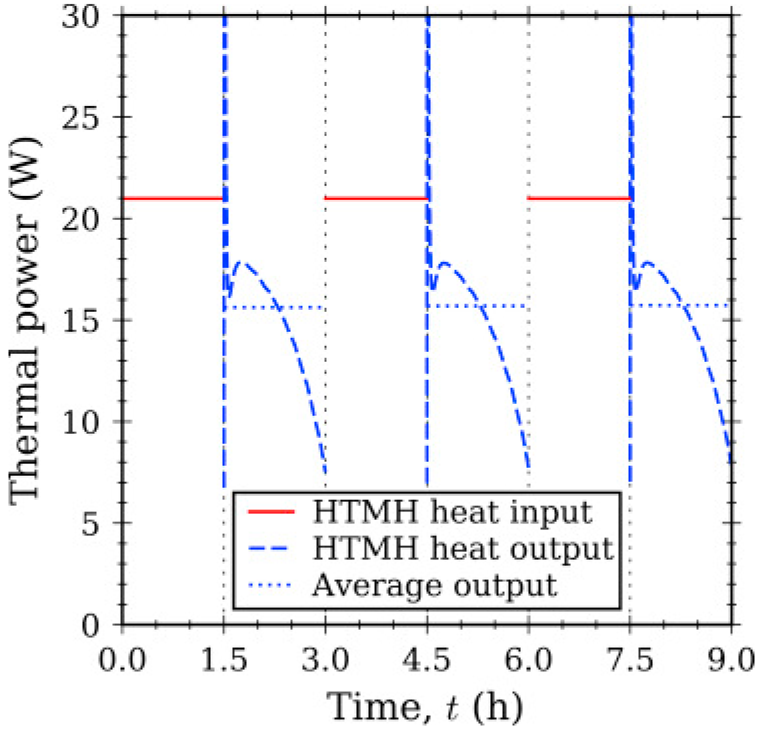

Figure 9: Heat input from heater to HTMH during LTMH charging and heat output from HTMH to vessel during HTMH charging as functions of time, as well as the time-averaged heat output. About 75% of the heat input during LTMH charging was returned during HTMH charging.

4.2.5 Thermal energy storage system heat transfer enhancements

Heat transfer limitations due to the relatively low thermal conductivity of the MH powders are expected to significantly limit system performance. There are several possible strategies for enhancing heat transfer in a paired-MH system, such as the inclusion of high-conductivity fins within the MH vessels or additives to the MH powder, such as expanded natural graphite, that increase the effective thermal conductivity of the mixture [7,21]. To examine the potential impacts on performance, the simulations described above were repeated with a tenfold increase in the effective thermal conductivities of the MH powders, i.e., increasing the values of k_{tot} to 5 W/m·K for the HTMH and 6 W/m·K for the LTMH. Such increases in conductivity have been demonstrated for other less conductive MH materials, such as $NaAlH_4$, by adding a small weight percent of expanded natural graphite in the metal hydride or compacting the MH material in pelletized form [21].

Figure 10 shows the average MH temperatures and local temperatures at selected locations as functions of time for (a) the LTMH and (b) the HTMH. The thermal conductivity enhancement in the MH beds substantially decreased both their internal temperature gradients and the overall variation in their average temperatures. The local temperatures ranged from 14°C to 32°C in the LTMH and from 640°C to 666°C in the HTMH (decreasing the temperature ranges by 11°C and 23°C, respectively). As before, the spatial temperature variation was larger in the HTMH than in the LTMH. This can be attributed to the fact that the reaction enthalpy ΔH and the resulting amount of thermal energy absorbed or released during operation is significantly larger for the HTMH.

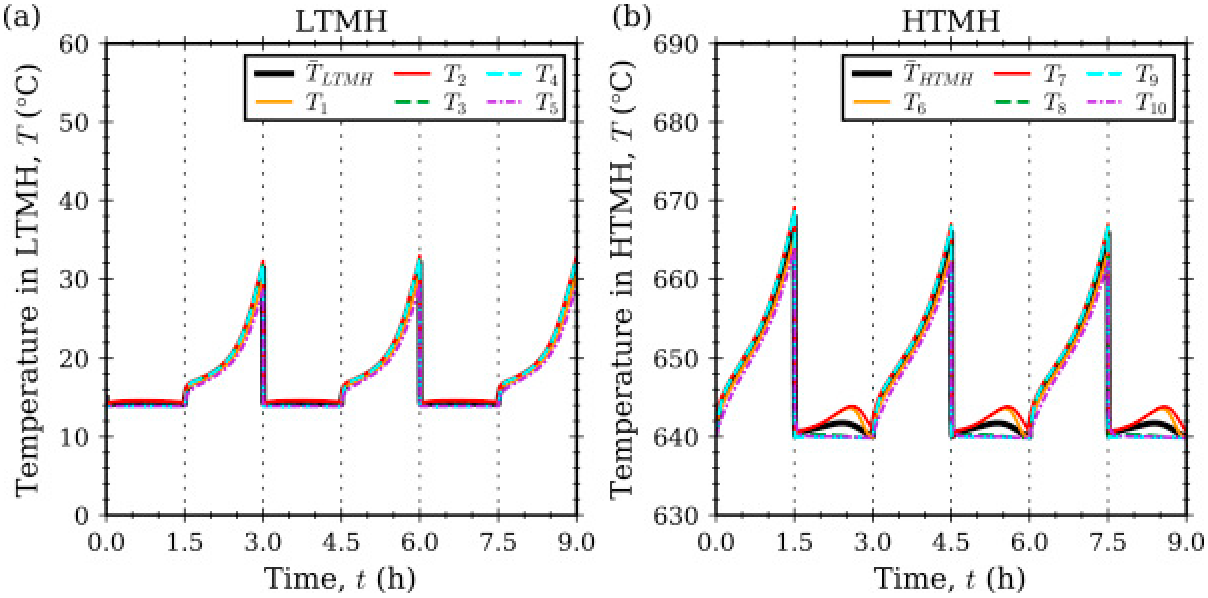

Figure 10: Average MH temperature and local temperatures for selected locations as a function of time in (a) the LTMH and (b) the HTMH for MHs with effective thermal conductivities enhanced by tenfold. The heat transfer enhancement substantially reduced both temperature gradients within the MH beds and the variation of the average temperature.

Figure 11 shows the gas pressure and the average equilibrium pressures in each MH bed. The enhanced thermal conductivities reduced the pressure variation over the cycle by more than half. The pressure ranged from 4.6 MPa to 5.4 MPa, a range of only 0.8 MPa in contrast to the 1.9-MPa range shown previously in Figure 4. During the HTMH discharging step, the gas pressure stayed roughly halfway between the average equilibrium pressures of the two beds. However, for the HTMH charging step, the gas pressure only slightly exceeded $\bar{P}_{HTMH}$, while $\bar{P}_{LTMH}$ was much larger than the gas pressure. The local equilibrium pressures (not shown), like the local temperatures shown in Figure 10, indicated small gradients and were close to the average values shown in Figure 11.

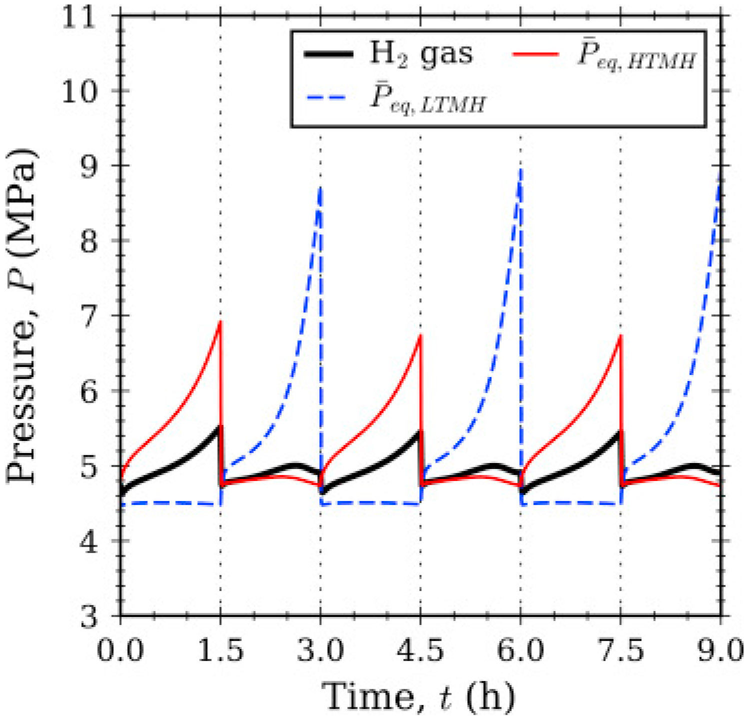

Figure 11: Pressure P of the hydrogen gas and average equilibrium pressures $\bar{P}_{eq,LTMH}$ and $\bar{P}_{eq,HTMH}$ for the LTMH and HTMH beds, respectively, as functions of time for system with enhanced MH thermal conductivities.

Figure 12 shows (a) the flowrate of H_2 gas leaving each MH bed and (b) the amount of H_2 contained in the LTMH, the HTMH, and the gas as functions of time. The flowrates during HTMH discharging were very similar to those observed previously in Figure 8(a). However, during HTMH charging, the enhanced heat transfer increased the peak flowrates near the beginning of the step, and the decrease in flowrate over the course of the step was steeper, approaching zero at the end of the step. Figure 12(b) reveals that the LTMH approached complete hydrogen depletion (reaching a minimum SOC of about 0.2%) and HTMH complete hydrogen saturation (maximum SOC of about 99.8%) by the end of the HTMH charging step. This accounts for the flowrates approaching zero and for the large increase in $\bar{P}_{LTMH}$ (Figure 11) required to continue desorbing hydrogen. The enhanced thermal conductivities enabled the system to cycle 83% of the hydrogen capacity in and out of the HTMH bed (an increase of 6% over the unenahnced system). Figure 12(b) demonstrates that HTMH discharging is the limiting step under these conditions. In the first cycle, for example, the HTMH was able to discharge only 81% of its hydrogen content during the HTMH discharging step, but the HTMH charging step restored both metal hydrides to their initial SOC about 15 minutes before the end of the step.

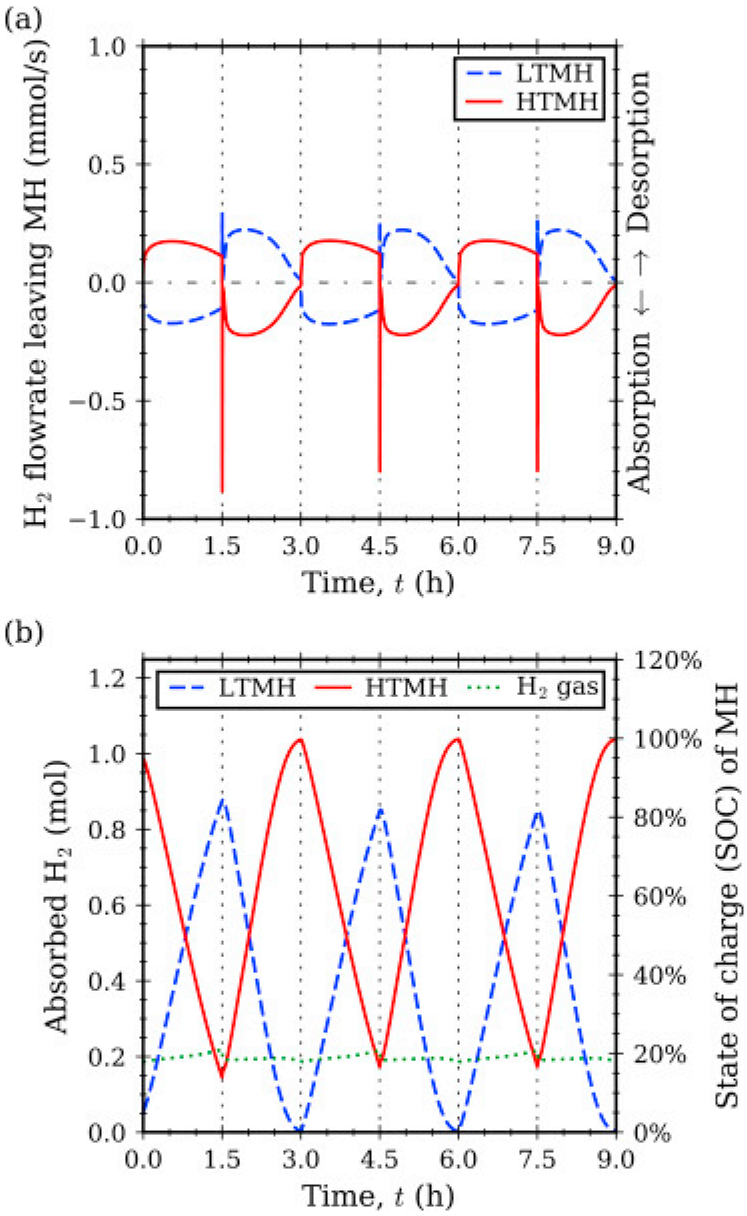

Figure 12: (a) The molar flowrate of H_2 gas exiting each MH bed and (b) the amount of H_2 stored in the HTMH, LTMH, and in gaseous form as functions of time. The corresponding state of charge of each MH is shown on the right-hand axis of (b).

Overall, the enhanced heat transfer simulations demonstrate that increasing the effective thermal conductivity of the MH beds significantly improved the system performance by decreasing temperature gradients within the beds, decreasing the variation in pressure and temperature over the cycle, while increasing the amount of H_2 transferred. The average HTMH heat output predicted for the enhanced-conductivity simulation was also increased, so that 80% of the heat input during LTMH charging was retrived during HTMH charging with an output energy density of 241 kWh/m^3, 9.7 times the SunShot target. The results also suggest that the selected metal hydride pair has good potential for achieving near 100% utilization of the metal hydride material and excellent thermal storage performance with further optimization of the vessel design and heat inputs.

5 Summary and conclusions

A detailed transport model was used to evaluate a metal hydride based thermal energy storage system coupled with an ultra-supercritical steam power plant. $NaMgH_2F$ and $TiCr_{1.6}Mn_{0.2}$ were selected as the high-temperature and low-temperature metal hydrides for the proposed system in order to supply turbine inlet temperatures on the order of 600°C at the high-temperature side of the storage system. In addition, the low temperature metal hydride material was demonstrated to be able to be coupled with the high temperature metal hydride at temperatures on the order of 15-30 °C, thus allowing the recovery of the steam power plant condenser waste heat. A bench-scale TES system was simulated to evaluate the performance of the MH pair, accounting for mass, momentum, and energy balances on the H_2 gas and the two MH beds. The model predicted successful cycling of 77% of the hydrogen capacity between the two metal hydrides with: (1) an output energy density of 226 kWh/m^3 (9 times the SunShot target value), (2) moderate temperature swings (<30°C in the LTMH and <50°C in the HTMH) and (3) pressure variation of only 1.9 MPa.

The effect of enhancing the heat transfer within the TES system was tested by increasing the effective thermal conductivities of the metal hydrides. The simulation results demonstrated that heat transfer enhancements can significantly improve the performance of the TES system. Without any further optimization other than the increased conductivities, both the output energy density and the fraction of hydrogen capacity utilized increased, while the temperature and pressure swings and the internal temperature gradients significantly decreased.

Overall, the results indicate that a TES system utilizing the proposed metal-hydride pair has the potential to provide large energy densities with near-100% utilization of the metal hydride capacity, and to operate in a suitable temperature range to couple with an ultra-supercritical steam power plant. Heat transfer limitations will be an important consideration in the TES system design in order to achieve good performance.

6 Acknowledgements

This work was performed as part of the DOE EERE SunShot Initiative. The authors wish to thank Drs. L. Irwin and A. Shultz, our project managers, in appreciation for their help and direction. The authors also wish to thank Drs D. Sheppard and C. Buckley of Curtin University for their help provided to characterize the high temperature material.

7 References

[1] Website: http://www.nrel.gov/docs/fy10osti/48658.pdf [accessed January 2017].

[2] Gil A, Medrano M, Martorell I, Lazaro A, Dolado P, Zalba B, et al. State of the art on high temperature thermal energy storage for power generation. Part 1 - Concepts, materials and modellization. Renew Sustain Energy Rev 2010;14:31-55.

[3] Stekli J, Irwin L, Pitchumani R. Technical challenges and opportunities for Concentrating Solar Power with Thermal Energy Storage. Journal of Thermal Science and Engineering Applications 2013;5:021011-1-12.

[4] Izquierdo S, Montanes C, Dopazo C, Fueyo N. Analysis of CSP Plants for the Definition of Energy Policies: The Influence on Electricity Cost of Solar Multiples, Capacity Factors and Energy Storage. Energy Policy 2010;38(10):6215-6221.

[5] Denholm P, Hand M. Grid Flexibility and Storage Required to Achieve Very High Penetration of Variable Renewable Electricity. Energy Policy 2011;39(3):1817-1830.

[6] Dominguez R, Baringo L, Conejo A. Optimal strategy for a concentrating solar power plant. Applied Energy 2012;98:316-325.

[7] Corgnale C, Hardy BJ, Motyka T, Zidan R, Teprovich J, Peters B. Screening analysis of metal hydride based thermal energy storage systems for concentrating solar power plants. Renew Sustain Energy Rev 2014;38:821-833.

[8] Corgnale C, Hardy B, Motyka T, Zidan R. Metal hydride based thermal energy storage system requirements for high performance concentrating solar power plants. Int J Hydrogen Energy 2016;41(44):20217-20230.

[9] Ward PA, Corgnale C, Teprovich JA, Motyka T, Hardy B, Sheppard D, et al. Technical challenges and future direction for high efficiency metal hydride thermal energy storage systems. Applied Physics A 2016;122:462.

[10] Sheppard DA, Paskevicius M, Humphries TD, Felderhoff M, Capurso G, Bellosta von Kolbe J, et al. Metal hydrides for concentrating solar thermal power energy storage. Applied Physics A 2016;122:395.

[11] Ward P, Corgnale C, Teprovich J, Motyka T, Hardy B, Peters B et al. High performance metal hydride based thermal energy storage systems for concentrating solar power applications" Journal of Alloys and Compounds 2015;645(1):S374-S378.

[12] Sheppard D, Corgnale C, Hardy B, Motyka T, Zidan R, Paskevicious M, et al. Hydriding characteristics of NaMgH2F with preliminary technical and cost evaluation of magnesium-based metal hydride materials for concentrating solar power thermal storage. RSC Advances 2014;4:26552-26562.

[13] Cziesla F, Bewerunge J, Senzel A. Lunen – state of the art Ultra Supercritical Steam Power Plant under construction. POWER-GEN Europe 2009, Cologne, Germany. Available online at https://www.energy.siemens.com/nl/pool/hq/power-generation/power-plants/steam-power-plant-solutions/coal-fired-power-plants/Luenen.pdf (accessed May 2017).

[14] General Electric Ultra-supercritical steam turbines. Available online at http://www.ge.com/in/thermal-power/steam-turbine-manufacturers (accessed May 2017).

[15] Bouamrane A, Laval JP, Soulie JP, Bastide JP. Structural characterization of $NaMgH_2F$ and $NaMgH_3$. Materials Research Bulletin 2000;35:545-549.

[16] Humphries TD, Sheppard DA, Rowles MR, Sofianos MV, Buckley CE. Fluoride substitution in sodium hydride for thermal energy storage applications. Journal Mater Chem A 2016;4:12170-12178.

[17] Website: http://webbook.nist.gov/chemistry/fluid/ [accessed November 2016].

[18] d’Entremont A, Corgnale C, Sulic M, Hardy BJ, Zidan R, Motyka T. Modeling of a thermal energy storage system based on coupled metal hydrides (magnesium iron – sodium alanate) for concentrating solar power plants. Int J Hydrogen Energy 2017;42(35):22518-29.

[19] Gamo T, Moriwaki Y, Yanagihara N, Yamashita T, Iwaki T. Formation and properties of titanium-manganese alloy hydrides. Int J Hydrogen Energy 1985;19(1):39-47.

[20] Zotov TA, Sivov RB, Movlaev EA, Mitrokhin SV, Verbetsky VN. IMC hydrides with high hydrogen dissociation pressure. Journal of Alloys and Compounds 2011;509S:839S-843S.

[21] Corgnale C, Hardy BJ, Tamburello DA, Garrison SL, Anton DL. Acceptability envelope for metal hydride-based hydrogen storage systems. Int J Hydrogen Energy 2012;37(3):2812-2824.

[22] Hardy BJ, Anton DL. Hierarchical methodology for modeling hydrogen storage systems. Part I: Scoping models. Int J Hydrogen Energy 2009;34(5):2269-2277.

[23] Hardy BJ, Anton DL. Hierarchical methodology for modeling hydrogen storage systems. Part II: Detailed models. Int J Hydrogen Energy 2009;34(7):2992-3004.